The Star Formation Rate of the Milky Way as Seen by Herschel

D. Elia[1] , S. Molinari[1] , E. Schisano[1] , J. D. Soler[1] , M. Merello[2] , D. Russeil[3] , M. Veneziani[4] , A. Zavagno[3,5] ,
A. Noriega-Crespo[6] , L. Olmi[7] , M. Benedettini[1] , P. Hennebelle[8] , R. S. Klessen[9,10] , S. Leurini[11] , R. Paladini[12] ,
S. Pezzuto[1] , A. Traficante[1] , D. J. Eden[13,14] , P. G. Martin[15] , M. Sormani[9] , A. Coletta[1,16] , T. Colman[8] ,
R. Plume[17] , Y. Maruccia[1] , C. Mininni[1] , and S. J. Liu[1]

[1] INAF—Istituto di Astrofisica e Planetologia Spaziali, Via Fosso del Cavaliere 100, I-00133 Roma, Italy; davide.elia@inaf.it
[2] Departamento de Astronomía, Universidad de Chile, Casilla 36-D, Correo Central, Santiago, Chile
[3] Aix Marseille Univ., CNRS, CNES, LAM, Marseille, France
[4] Science & Technology Corporation, Olof Palmestraat 14, 2616 LR Delft, The Netherlands
[5] Institut Universitaire de France, Paris, France
[6] Space Telescope Science Institute, 3700 San Martin Dr., Baltimore, MD 21218, USA
[7] INAF—Osservatorio Astrofisico di Arcetri, Largo E. Fermi 5, I-50125, Firenze, Italy
[8] Université Paris-Saclay, Université Paris Cité, CEA, CNRS, AIM, F-91191, Gif-sur-Yvette, France
[9] Universität Heidelberg, Zentrum für Astronomie, Institut für theoretische Astrophysik, Albert-Ueberle-Str. 2, D-69120 Heidelberg, Germany
[10] Universität Heidelberg, Interdiszipliäres Zentrum für Wissenschaftliches Rechnen, Im Neuenheimer Feld 205, D-69120 Heidelberg, Germany
[11] INAF—Osservatorio Astronomico di Cagliari, Via della Scienza 5, I-09047 Selargius (CA), Italy
[12] Infrared Processing Analysis Center, California Institute of Technology, Pasadena, CA 91125, USA
[13] Astrophysics Research Institute, Liverpool John Moores University, IC2, Liverpool Science Park, 146 Brownlow Hill, Liverpool, L3 5RF, UK
[14] Armagh Observatory and Planetarium, College Hill, Armagh, BT61 9DB, UK
[15] Canadian Institute for Theoretical Astrophysics, University of Toronto, 60 St. George Street, Toronto, ON, M5S 3H8, Canada
[16] Dipartimento di Fisica, Sapienza Università di Roma, Piazzale Aldo Moro 2, I-00185, Rome, Italy
[17] Department of Physics & Astronomy, University of Calgary, 2500 University Dr. NW, Calgary, AB, T2N 1N4, Canada

Abstract

We present a new derivation of the Milky Way's current star formation rate (SFR) based on the data of the Herschel InfraRed Galactic Plane Survey (Hi-GAL). We estimate the distribution of the SFR across the Galactic plane from the star-forming clumps identified in the Hi-GAL survey and calculate the total SFR from the sum of their contributions. The estimate of the global SFR amounts to $2.0 \pm 0.7 \, M_\odot \, \mathrm{yr}^{-1}$, of which $1.7 \pm 0.6 \, M_\odot \, \mathrm{yr}^{-1}$ coming from clumps with reliable heliocentric distance assignment. This value is in general agreement with estimates found in the literature of last decades. The profile of SFR density averaged in Galactocentric rings is found to be qualitatively similar to others previously computed, with a peak corresponding to the Central Molecular Zone and another one around Galactocentric radius $R_{\mathrm{gal}} \sim 5 \, \mathrm{kpc}$, followed by an exponential decrease as $\log(\Sigma_{\mathrm{SFR}}/[M_\odot \, \mathrm{yr}^{-1} \, \mathrm{kpc}^{-2}]) = a \, R_{\mathrm{gal}}/[\mathrm{kpc}] + b$, with $a = -0.28 \pm 0.01$. In this regard, the fraction of SFR produced within and outside the solar circle is 84% and 16%, respectively; the fraction corresponding to the far outer Galaxy ($R_{\mathrm{gal}} > 13.5 \, \mathrm{kpc}$) is only 1%. We also find that, for $R_{\mathrm{gal}} > 3 \, \mathrm{kpc}$, our data follow a power law as a function of density, similarly to the Kennicutt–Schmidt relation. Finally, we compare the distribution of the SFR density across the face-on Galactic plane and those of median parameters, such as temperature, luminosity/mass ratio, and bolometric temperature, describing the evolutionary stage of Hi-GAL clumps. We found no clear correlation between the SFR and the clump evolutionary stage.

Unified Astronomy Thesaurus concepts: Star formation (1569); Milky Way Galaxy (1054); Far infrared astronomy (529); Galaxy structure (622)

1. Introduction

The star formation rate (SFR) is a widely used parameter to globally characterize galaxies (see Kennicutt & Evans 2012, and references therein). In the absence of small-scale description of the star-forming activity in external galaxies, their SFR expresses the fundamental relationship between the stellar mass and the gas reservoir on which our understanding of galaxy formation and evolution is based (see, e.g., McKee & Ostriker 2007; Krumholz 2014).

Several estimates of the SFR have been computed for the Milky Way as well. Considering, in principle, the total mass of available molecular gas and the freefall time in typical conditions

of clouds in the Galaxy would lead to a prediction of a global SFR of $300 \, M_\odot \, \mathrm{yr}^{-1}$ (reducible to $46 \, M_\odot \, \mathrm{yr}^{-1}$ if only bound clouds are considered; Evans et al. 2021). However, the actual estimates based on direct star formation indicators converge toward a value of a few $M_\odot \, \mathrm{yr}^{-1}$ (see Licquia & Newman 2015, and references therein). As shown by Fraser-McKelvie et al. (2019) and Boardman et al. (2020), this is a typical SFR for galaxies with characteristics similar to those of the Milky Way, while in different galaxies values up to a few tens of $M_\odot \, \mathrm{yr}^{-1}$ can be reached (see, e.g., Chomiuk & Povich 2011; Mutch et al. 2011).

State-of-the-art estimates of the SFR, summarized in Table 1, provide an illustration of the variations found using different methods. The previous compilation, presented in Chomiuk & Povich (2011, their Table 1), renormalized some of the archival values from the literature, to conform all of them to the same initial mass function (IMF; Kroupa & Weidner 2003; Kennicutt et al. 2009), as also recommended by Davies et al. (2011).

Table 1
Star Formation Rate Estimates for the Milky Way

Method	SFR ($M_\odot$ yr^{-1})	References
Ionization rate from radio free–free	0.35[a]	Smith et al. (1978)
Ionization rate from radio free–free	2.0 ± 0.6[a]	Guesten & Mezger (1982)
Ionization rate from radio free–free	1.6 ± 0.5[a]	Mezger (1987)
Ionization rate from [N II] 205 μm (COBE)	2.6 ± 1.3[a]	Bennett et al. (1994)
Ionization rate from [N II] 205 μm (COBE)	2.0 ± 1.0[a]	McKee & Williams (1997)
O/B star counts	1.8 ± 0.6[a]	Reed (2005)
Nucleosynthesis from ^{26}Al (INTEGRAL)	2.0 ± 1.2[a]	Diehl et al. (2006)
Continuum emission at 100 μm (COBE)	1.9 ± 0.8[a]	Misiriotis et al. (2006)
Ionization rate from microwave free–free (WMAP)	2.4 ± 1.2[a]	Murray & Rahman (2010)
YSO counts (Spitzer)	1.1 ± 0.4[a]	Robitaille & Whitney (2010)
YSO counts (MSX)	1.8 ± 0.3	Davies et al. (2011)
Combination of literature values	1.9 ± 0.4	Chomiuk & Povich (2011)
Continuum emission at 70 μm (Herschel)	2.1 ± 0.4	Noriega-Crespo (2013)
Combination of literature values	1.65 ± 0.19	Licquia & Newman (2015)
FIR clump counts (Herschel)	2.0 ± 0.7	This work

Note.
[a] This value is not taken from the original article, but was rescaled by Chomiuk & Povich (2011) to normalize all literature results to the same IMF (see text).

Misiriotis et al. (2006), using a direct relation between COBE/DIRBE 100 μm emission and SFR already adopted for external galaxies, provided a value of 2.7 $M_\odot$ yr^{-1} for the Milky Way's SFR. Robitaille & Whitney (2010) estimated a SFR from 0.68 to 1.45 $M_\odot$ yr^{-1}, starting from young stellar objects (YSOs) revealed in the Spitzer/IRAC GLIMPSE Galactic plane survey, and using model spectral energy distributions (SEDs) to predict the brightness and color of the synthetic YSOs at different wavelengths.

More recent results do not use new data sets but are derived by reconsidering values existing in the literature: Chomiuk & Povich (2011) determine a SFR of 1.9 ± 0.4 $M_\odot$ yr^{-1} by combining and renormalizing literature results from 1978 to 2011. Licquia & Newman (2015) derived a SFR of 1.65 ± 0.19 $M_\odot$ yr^{-1} by statistically combining the prior measurements of this quantity in the literature through a hierarchical Bayesian method.

An independent estimate of the SFR can be given through a technique which uses far-IR (FIR) Herschel[18] satellite (Pilbratt et al. 2010) data, and in particular photometric observations carried out by its Photodetector Array Camera and Spectrometer (PACS, at 70 and 160 μm; Poglitsch et al. 2010) and Spectral and Photometric Imaging Receiver (SPIRE, at 250, 350, and 500 μm; Griffin et al. 2010) cameras. Veneziani et al. (2013) developed such a method that starts from the compact sources detected in Herschel maps. They generally correspond to unresolved clumps that already host active star formation, or, alternatively, are starless but show conditions for future activity. By considering the former category of sources, Veneziani et al. (2013) evaluated the contribution of each individual clump to the total SFR in two $2° \times 2°$ tiles of Herschel InfraRed Galactic Plane Survey (Hi-GAL; Molinari et al. 2010), namely the Open Time Key Project for unbiasedly surveying the whole Galactic plane with PACS and SPIRE. For comparison, they also derived the SFR of the same two regions through the method of Li et al. (2010) based on assuming a direct relation between SFR and 70 μm emission.

Subsequently, by assuming that these two fields are representative of the entire Milky Way, Noriega-Crespo (2013) extrapolated for the entire Galactic SFR an estimate of 2.1 ± 0.4 $M_\odot$ yr^{-1}.

Other works also discussed the profile of the Milky Way SFR as a function of the Galactocentric distance, R_{gal}, both to quantify the ability of different zones of our Galaxy to form stars and to make a comparison with external galaxies, for which this relation is observed. A typical approach is to study the SFR density, averaged in concentric Galactic rings, as a function of the middle radius of the ring (e.g., Guesten & Mezger 1982; Portinari & Chiosi 1999; Kennicutt & Evans 2012; Lee et al. 2016). It is generally seen that the profile of this quantity has an absolute maximum in correspondence of the Central Molecular Zone (CMZ), another local maximum around at $R_{gal} \sim 4$–5 kpc (with a dip in the middle, centered at $R_{gal} \sim 2$ kpc), and an exponential decrease at larger radii.

In this paper, by extending the method of Veneziani et al. (2013), refined by Veneziani et al. (2017), to the clump catalog of the entire Hi-GAL survey, we present a direct and self-consistent estimate of the SFR for the whole Milky Way, illustrating both the global SFR and its distribution across the Galactic plane.

In Section 2 we show how Hi-GAL protostellar clump properties can be used to obtain an estimate of the current Galactic SFR. In Section 3 we discuss how the SFR is distributed across the Milky Way, adopting both the [ℓ, b] and the pole-on perspective. We also make a test of the Kennicutt–Schmidt (KS) law with our data, and investigate possible links between local SFR and clump average evolutionary stage. Finally, in Section 4 we draw our conclusions.

2. The Herschel-based Milky Way's Star Formation Rate Estimation

2.1. Source Selection

We calculated the Galactic SFR using the physical properties of clumps identified in the Hi-GAL survey (Elia et al. 2021). These objects were identified and cataloged as follows.

The detection and five-band photometry of Hi-GAL compact sources (i.e., unresolved or poorly resolved) were performed through the CuTEx algorithm (Molinari et al. 2011) in the five Hi-GAL bands, to obtain the single-band catalogs presented by Molinari et al. (2016) and S. Molinari et al. (2022, in preparation).

Starting from these lists, Elia et al. (2021) obtained a band-merged catalog, from which only SEDs with a shape eligible for a modified blackbody fit in the range from 160 to 500 μm were selected (further details can be also found in Elia et al. 2013, 2017).

Heliocentric distances were estimated by Mège et al. (2021) in three steps: (i) by extracting the most reliable velocity component along the line of sight from available spectroscopic surveys of the Galactic plane; (ii) by applying the rotation curve of Russeil et al. (2017) and solving the near/far distance ambiguity toward the inner Galaxy by considering H I absorption; and (iii) by complementing this information with independent estimates such as HII region distances or maser parallaxes. The medians of the absolute and relative error on distances of Mège et al. (2021) are 0.54 kpc and 16%, respectively.

As pointed out in Elia et al. (2017, 2021), the Hi-GAL compact sources are distributed along a wide range of heliocentric distances and consequently achieve a variety of physical sizes corresponding to different kinds of structures: from single cores to larger overdensities hosting a more complex but unresolved morphology. In particular, the majority of Hi-GAL sources fulfill the definition of clump based on physical diameter ($0.3 < D < 3$ pc; Bergin & Tafalla 2007).

As a rough criterion to classify the clumps in star-forming versus quiescent (designated for brevity as protostellar and starless, respectively), Elia et al. (2021) adopted the availability/lack of a detection at 70 μm, respectively.

The modified blackbody fit provided temperatures for the clump SEDs and, for cases with an available distance estimate, also the mass and the bolometric luminosity. The mass was used to further classify the starless clumps as gravitationally bound (called pre-stellar) versus unbound, by using a gravitational stability criterion based on the so-called third Larson's relation (Larson 1981). For pre-stellar sources the luminosity was estimated from the whole integral of the best-fitting modified blackbody. For protostellar sources, generally showing an excess of emission at $\lambda < 70$ μm with respect to the modified blackbody (e.g., Dunham et al. 2008; Giannini et al. 2012; Elia et al. 2017), the luminosity is estimated by considering the sum of the integrals of the observed SED for $\lambda < 160$ μm and of the best-fitting modified blackbody for $\lambda \geqslant 160$ μm, respectively.

The same considerations made above about the physical size can be extended to the other distance-dependent observables, mass and luminosity. Their ranges of variability extend over several orders of magnitude not only due to intrinsic differences among objects (that can be appreciated among sources located at the same distance), but also—and above all—due to the wide range of underlying distances, as Figures 9 and 13 of Elia et al. (2021) clearly illustrate. More quantitatively, 99% of the Hi-GAL clumps of Elia et al. (2021) provided with a distance estimate have masses ranging from 0.1 to 10^4 $M_\odot$ and luminosities ranging from 0.1 to 10^5 $L_\odot$.

To compute the SFR through the method described in Section 2.2, first we consider all 29,880 protostellar clumps provided with a heliocentric distance. Subsequently, in Section 2.2.1 we evaluate and suggest a reasonable additional term which accounts for the contribution by a further 5532 protostellar clumps lacking a distance determination.

2.2. Computation of the Star Formation Rate

To determine the SFR we followed the method described by Veneziani et al. (2013) and refined by Veneziani et al. (2017).

In short, the contribution of each protostellar source to the total SFR is computed through theoretical evolutionary tracks reported in the bolometric luminosity versus mass diagram (Molinari et al. 2008; Baldeschi et al. 2017b; Elia et al. 2021). At each time step, together with the clump mass–luminosity pair, the mass of the internal protostar being formed is also computed. At the end point of the theoretical track both the final mass of the star and the corresponding total elapsed time are known. The ratio between these two quantities constitutes the SFR contribution from the given clump.

The evolutionary tracks were initially obtained by Molinari et al. (2008) for the case of an object forming a single central star but, especially at higher masses, we actually deal with clumps possibly hosting the formation of entire protoclusters (e.g., Baldeschi et al. 2017a). Veneziani et al. (2017) took into consideration this aspect by applying a Monte Carlo procedure to an evolutionary model of turbulent cores to account for the wide multiplicity of sources produced during the clump collapse. We implemented this refinement in this work as well (for details, see Veneziani et al. 2017).

Furthermore, given the wide range of clump heliocentric distances quoted in the Hi-GAL catalog (Elia et al. 2017, 2021), a distance bias might be expected to affect the estimate of physical parameters for these objects. Baldeschi et al. (2017a) proposed a method to evaluate this possible bias by simulating the appearance of nearby star-forming regions observed by the Herschel Gould Belt Survey (André et al. 2010) if they were moved to larger distances (from 0.75 to 7 kpc), comparable to those typically found in the Hi-GAL survey. Subsequently, in Baldeschi et al. (2017b) this approach was applied, in particular, to the estimation of the SFR. For three nearby regions they compared the SFR obtained from YSO counts (based on an updated version of Equation (1) of Lada et al. 2010) to that estimated through the method of Veneziani et al. (2017) from the clumps detected in the Herschel maps "displaced" at different virtual distances. They found that the two estimates remain consistent with each other within a factor 2 at various probed distances.

Based on these premises we feel confident to adopt the method of Veneziani et al. (2017). As mentioned above, the output of the algorithm we used is the contribution of each clump, Σ_{cl}, to the global SFR. This quantity depends on the evolutionary track in the L/M plot, which, in turn, is defined by the initial clump mass, M_{cl}. Although not explicitly stated in the original articles, this algorithm associates the final star mass to the input clump mass by interpolating the locus of final masses of known evolutionary tracks with a power law. Here we explicitly report the corresponding formula we used:

$$\mathrm{SFR}_{cl} = (5.6 \pm 1.4) \times 10^{-7} \, (M_{cl}/M_\odot)^{0.74 \pm 0.03} \, M_\odot \, \mathrm{yr}^{-1}. \quad (1)$$

We propose this relation hereafter as an operational prescription for an immediate application of the method of Veneziani et al. (2017).

The global SFR, estimated by adding up all these contributions, amounts to $1.7 \pm 0.6\,M_\odot\,\mathrm{yr}^{-1}$. The uncertainty is given by the error propagation, combining in quadrature the uncertainties affecting the clump masses and the parameters appearing in Equation (1).

Adopting a classification of inner versus outer Galaxy delimited by the solar circle with a radius of 8.34 kpc (as in Elia et al. 2021; Mège et al. 2021), it is possible to give separately the contributions to the global SFR from these two zones: 1.5 (i.e., the 84% of the total) and $0.3\,M_\odot\,\mathrm{yr}^{-1}$ (16%), respectively.

2.2.1. Contribution from Sources Devoid of a Distance Estimate

It should be noted that the SFR estimate reported above is intended as a lower limit, since the input data, namely the protostellar clump list, is incomplete for the reasons described in the following. First, since the mass completeness in the Hi-GAL catalog is a function of the heliocentric distance (Elia et al. 2017), faint and/or far and/or cold protostellar clumps might remain undetected at all. We address this issue in Appendix A. Second, protostellar clumps undetected at 70 μm (for the same reasons written above), but detected at the other ones, result in a misclassification as starless and are not involved in the SFR calculation. In fact, in the literature examples can be found of spectroscopic signatures of active star formation detected in 70 μm dark clumps (e.g., Traficante et al. 2017). Third, 5532 sources classified as protostellar in the Hi-GAL catalog are not provided with a distance, and consequently are not involved in our previous calculation (see Figure 1).

Regarding the last point, it is possible to give an estimate of the missing contribution from this subsample by simulating a plausible realization of distances for sources whose distance is unknown. In this way, masses can be obtained also for them, to be inputted in the SFR calculation.

We simulated a set of 5532 distances whose distribution follows the one of the protostellar sources provided with a distance estimate. Then we randomly assigned each simulated distance to a clump devoid of distance, computed mass and luminosity accordingly, and estimated the contribution to the SFR with the usual procedure. This random assignation of distances to clumps has been repeated 100 times (two of which are shown in Figure 2), to keep safe from specific effects possibly induced by a single realization. The 100 corresponding estimates of additional SFR contribution are found to be confined in the relatively narrow range 0.20–$0.23\,M_\odot\,\mathrm{yr}^{-1}$, with an average of $0.22\,M_\odot\,\mathrm{yr}^{-1}$ and a standard deviation of $0.01\,M_\odot\,\mathrm{yr}^{-1}$. Notice that this standard deviation is expected to decrease by increasing the number of simulation as desired. The real uncertainty, instead, is dominated by the typical error bar associated to the SFR contribution evaluated for each simulation, which is $0.08\,M_\odot\,\mathrm{yr}^{-1}$.

In conclusion, a reasonable estimate of the total Galactic SFR, taking into account the correction calculated above, is $2.0 \pm 0.7\,M_\odot\,\mathrm{yr}^{-1}$.

The above test is based on the assumption that the real (unknown) distances of sources lacking this information follow the same distribution of the known ones. However, the lack of a distance estimate, i.e., the impossibility of individuating a clear and/or reliable spectral component along the line of sight of the Hi-GAL source (Mège et al. 2021), could be, in principle, due to specific local conditions. This could then produce a departure from the assumed behavior of distance distributions.
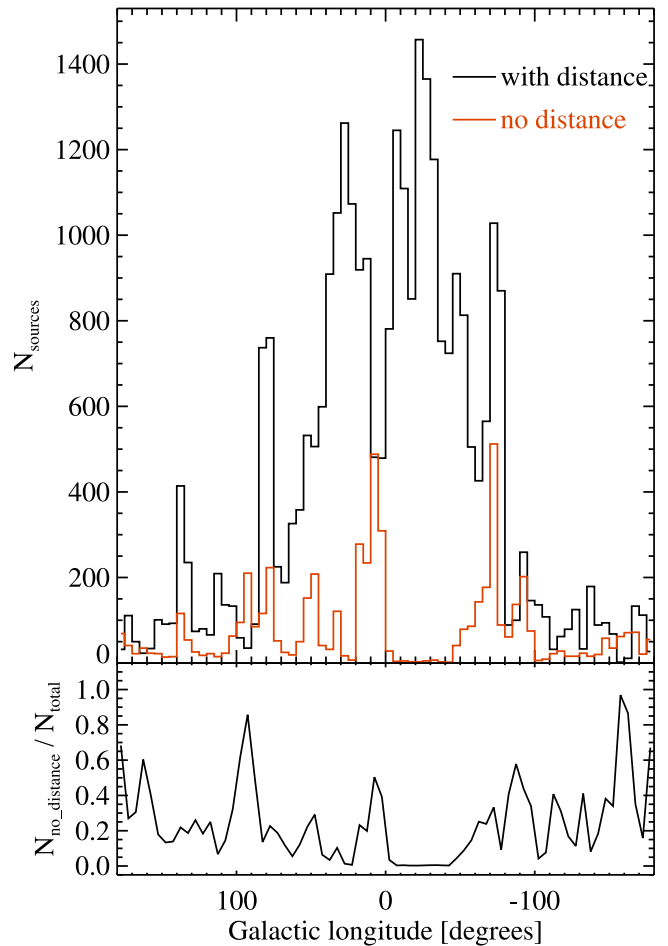

Figure 1. Top: distributions of Hi-GAL protostellar clumps with and without a heliocentric distance estimate (black and red histograms, respectively) in 5° wide bins of Galactic longitude. Bottom: number ratio between protostellar clumps without a distance estimate and the total number, in the same longitude bins as in the top panel.
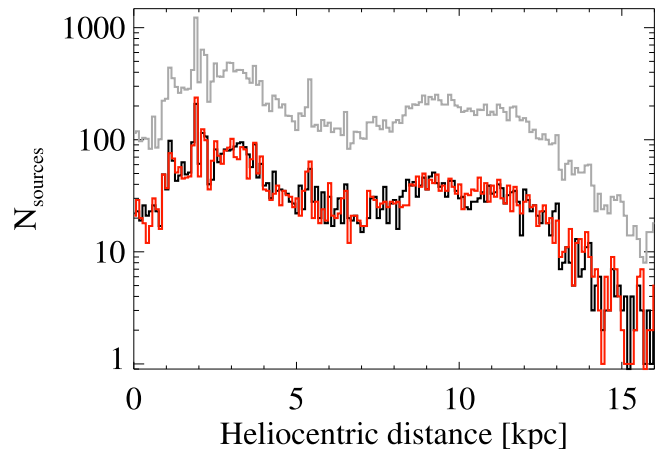

Figure 2. Two examples (black and red histograms, respectively, in bins of 100 pc) of realizations of heliocentric distance distributions to be assigned, as a test, to Hi-GAL protostellar clumps devoid of a distance estimate, compared with the distance distribution for sources provided with a distance estimate (gray histogram; Elia et al. 2021).

In this respect, the most unfavorable hypothetical case would be to have all sources located at the same distance. Therefore, supposing that all sources without distance were located at a minimum and at a maximum distance, respectively, helps us to
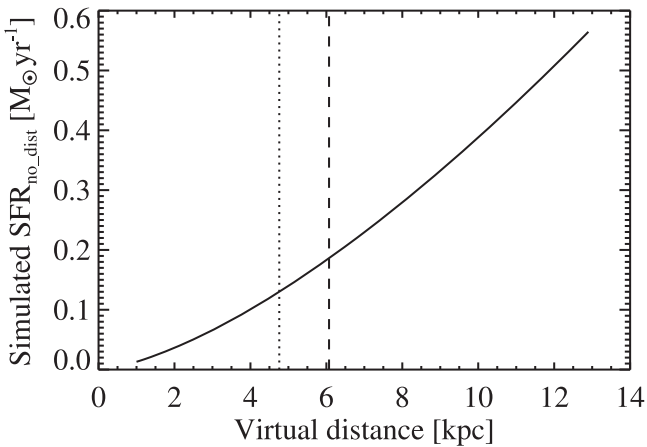
Figure 3. Probable contribution to the overall SFR from sources lacking a distance estimate if they were all located at the same virtual distance. The dotted and dashed lines represent the median and the average of the real distance distribution, respectively.

identify a range of maximum variability of their contribution to the total SFR. We therefore analyzed the behavior of such contribution for a common distance varying between 1 and 13 kpc (these limits are suggested by the distributions shown in Figure 2). From Figure 3 we see that for a virtual common distance of 1 kpc the contribution to the SFR would be negligible, while for 13 kpc it would amount to $0.57\,M_\odot\,\mathrm{yr}^{-1}$. Clearly, both scenarios (and, consequently, the corresponding contributions to SFRs) are unrealistic, but this test proves that, even in the case of an extremely unfavorable distance distribution of clumps without distance assignment, the order of magnitude of the SFR increment estimated through our test would be confirmed. Finally, we notice that, assuming that all sources without known distance were placed at the median and the average of the known distance distribution, their contribution would amount to 0.13 and $0.19\,M_\odot\,\mathrm{yr}^{-1}$, respectively (see Figure 3).

A final test we propose consists in a hybrid approach between the two followed above. Indeed, the top panel of Figure 1 suggests that the distribution in longitude of clumps lacking a distance assignment is far from being uniform and, moreover, it does not strictly follow the behavior of sources with a distance (as testified by the high degree of scatter of the ratio between the former distribution and the overall one, shown in the bottom panel). Statistically significant amounts of sources without a distance are found in correspondence of the innermost Galactic longitudes ($0° \lesssim \ell \lesssim 20°$), and in the direction of the Carina Arm ($270° \lesssim \ell \lesssim 310°$). The first case can be treated with relative ease, by arbitrarily placing all the sources without distance and with $|\ell| < 20°$ at the Galactic center distance of 8.34 kpc, and proceeding for the remaining sources by simulating distances distributed as the known ones. In this case, the additional term to the global SFR would amount to $0.17 \pm 0.06\,M_\odot\,\mathrm{yr}^{-1}$.

2.3. Comparison with the Previous Literature

Adopting the value of $2.0 \pm 0.7\,M_\odot\,\mathrm{yr}^{-1}$ as our final estimate for the Milky Way SFR, and comparing with the values in Table 1, it can be seen that it is consistent, within the error bars, with all but one (namely Smith et al. 1978) estimates collected and normalized by Chomiuk & Povich (2011), and with the estimates of Chomiuk & Povich (2011) themselves

and of Licquia & Newman (2015). Remarkably, our estimate is also perfectly consistent, within the errors, with that of Noriega-Crespo (2013), confirming that his choice to extrapolate the SFR estimate from an area of 8 sq. deg. to the entire 720 sq. deg was quite reasonable.

Our result, in essence, corroborates the common idea—supported by the fact that a variety of approaches leads to similar values—that the current SFR of the Milky Way lies in the range 1.5–2.5 $M_\odot\,\mathrm{yr}^{-1}$, which is consistent with the values found for spiral galaxies (e.g., Kennicutt & Evans 2012).

3. The Star Formation Rate across the Galactic Plane

We studied the SFR distribution across the Galactic plane. From here on, we will only consider the contribution to SFR given by clumps whose heliocentric distance is known, for which the position in the Galaxy can be determined.

3.1. Mapping Star Formation Rate in Galactic Coordinates: The Central Molecular Zone

A first view of SFR distribution in the Galactic plane can be given in the $[\ell, b]$ plane, as shown in Figure 4, top. It can be seen that, approximately, most of the total SFR (90%) comes from the inner 120° (Figure 4, bottom).

For the used binning of 3° in longitude and 0.2° in latitude, the three most prominent local maxima are found in pixels corresponding to the ranges $336° < \ell < 339°$ and $-0.2° < b < 0.0°$ (containing the G337.342–0.119 region; Jackson et al. 2018), $27° < \ell < 30°$ and $0.0° < b < 0.2°$, and $18° < \ell < 21°$ and $-0.2° < b < 0.0°$, respectively.

Through the $[\ell, b]$ view of the Galactic SFR it is also possible to make a direct comparison with SFRs estimated in the literature for the CMZ, generally taken as a rectangular coordinate box in such plane. In Table 2 we report a list of recent $\mathrm{SFR}_{\mathrm{CMZ}}$ estimates, each of them derived in a different area around the Galactic center, and the output of our method for the same area.

We found a good agreement with the $\mathrm{SFR}_{\mathrm{CMZ}}$ estimates reported in Crocker et al. (2011) and Immer et al. (2012). We also found a fairly good agreement with Barnes et al. (2017) on $\mathrm{SFR}_{\mathrm{CMZ}}$, which those authors estimated from monochromatic fluxes or bolometric luminosities available in the literature from 1998 to 2011, and ranging from 0.07 to $0.12\,M_\odot\,\mathrm{yr}^{-1}$, to be compared with our estimate of $0.06 \pm 0.02\,M_\odot\,\mathrm{yr}^{-1}$.

Our results, however, appear to disagree with the SFRs estimated for the CMZ in Yusef-Zadeh et al. (2009) and Longmore et al. (2013). The $\mathrm{SFR}_{\mathrm{CMZ}}$ in Yusef-Zadeh et al. (2009) is above our result, which is most likely due to an excessive number of early YSOs involved in the calculation, as discussed in Koepferl et al. (2015), who quantify this overestimate in a factor of 3. Correcting by this factor, the estimate of Yusef-Zadeh et al. (2009) would turn out to be consistent with our value ($0.04 \pm 0.02\,M_\odot\,\mathrm{yr}^{-1}$) within the uncertainties.

Longmore et al. (2013) estimated $\mathrm{SFR}_{\mathrm{CMZ}} = 0.035\ M_\odot\,\mathrm{yr}^{-1}$ in the range $2.5° < \ell < 3.5°$ and $|b| < 0.5°$, and $0.06\,M_\odot\,\mathrm{yr}^{-1}$ if the wider latitude range $|b| < 1°$ is considered in the central $|\ell| < 1°$. Correspondingly, we calculate $\mathrm{SFR}_{\mathrm{CMZ}} = 0.11$ and $0.12\,M_\odot\,\mathrm{yr}^{-1}$ for these two zones, respectively. The former one is about three times larger than that of Longmore et al. (2013), and not compatible with it within the associated error bar. Of course, the estimate of Longmore et al. (2013) is also the
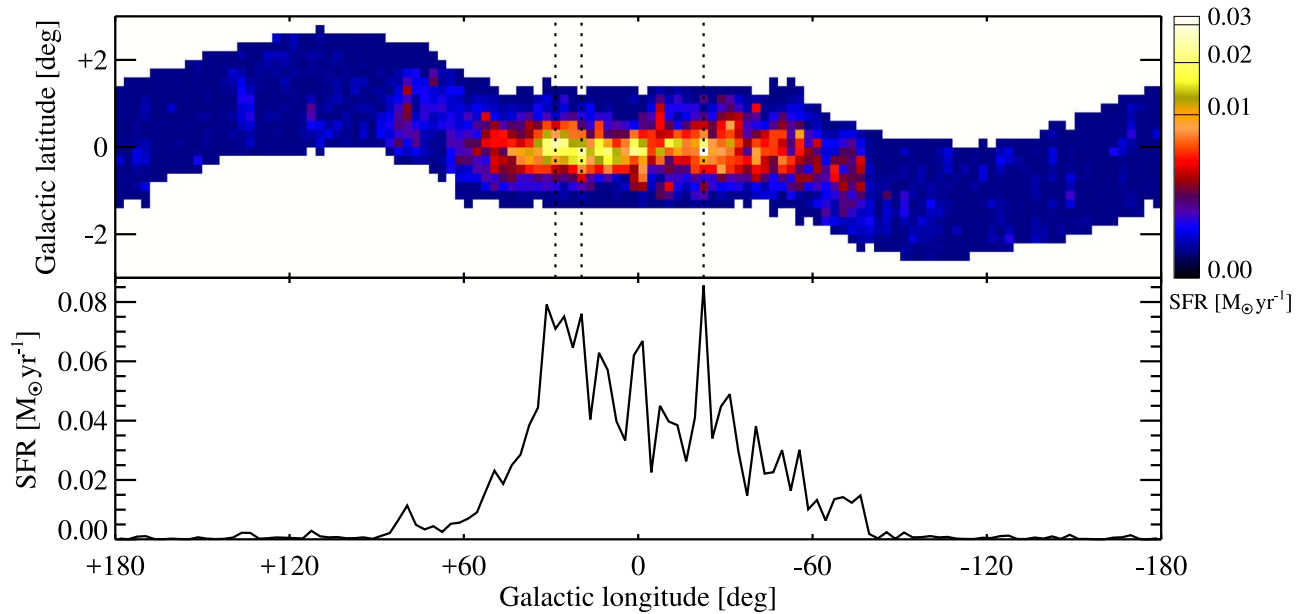
Figure 4. Top: star formation rate (SFR) toward the Galactic plane in $3° \times 0.2°$ bins in Galactic longitude and latitude, respectively. It should be noted that in the outer Galaxy the Hi-GAL latitude coverage follows the variations in the midplane position, or Galactic warp (Westerhout 1957). For a better rendering of the image dynamic range, the color scale follows a power law with exponent 0.4. The dotted lines indicate the location of the three most prominent SFR peaks. Bottom: SFR as a function of longitude, estimated from the sum of the results reported in the top panel across Galactic latitude.

lowest among the estimates from the literature collected in Table 2. The authors indeed suggest that the choice of the assumed IMF, which did not account for possible peculiar conditions of the CMZ, could affect this estimate down to a factor of $1/3$.

3.2. Star Formation Rate Galactocentric Profile

Using the information about the heliocentric distance, a pole-on view of SFR density in the Milky Way, mapped on a grid of $0.5 \times 0.5 \, \text{kpc}^2$ pixels, can be built. This is a simplified 2D representation of the Galactic disk, which has a structure along the third dimension, an idea of which can be taken from Figure 4. The design of the Hi-GAL survey took into account the warp of FIR emission already observed by IRAS toward the outer Galaxy, which however is less prominent than the Galactic warp observed in atomic gas (Westerhout 1957; Soler et al. 2022), corresponding to Galactocentric distances not achieved by objects in our sample ($R_{\text{gal}} \gtrsim 16 \, \text{kpc}$; Voskes & Butler Burton 2006).

In Figure 5 one can appreciate that, with respect to the Galactic center (to which we assign the [0, 0] position), the SFR shows a certain degree of circular symmetry.

It makes sense, therefore, to analyze the behavior of the SFR density Σ_{SFR}, averaged in concentric 500 pc wide rings, versus the Galactocentric radius R_{gal}. In Figure 6, top panel, a peak corresponding to the inner circle[19] is followed by a wide dip between 1 and 4 kpc, mostly due to a shortage of sources at these Galactocentric distances (Elia et al. 2021). This is seen also in other works (see below), and is due in part to the lack of SFR data in two lobes extending southwest and southeast of the

Galactic center position over an extent of about 4 kpc (recognizable as inner void areas in Figure 5), which can not be populated with heliocentric distances since the observed clump velocities are forbidden by the adopted rotation curve (Russeil et al. 2017). In particular, in these areas absolute values of radial velocity are expected to be larger than $100 \, \text{km s}^{-1}$ (Ellsworth-Bowers et al. 2015, their Figure 1), while most of the sources observed in the corresponding longitude ranges show lower values. The kinematics of the Milky Way along these lines of sight is indeed generally dominated by the Galactic bar (Binney et al. 1991; Ellsworth-Bowers et al. 2015; Li et al. 2016). As explained by Mège et al. (2021) and Elia et al. (2021), only in cases of small deviations, the distance of the corresponding tangent point is assigned to sources, which can therefore be involved in the calculation of the SFR. Additionally, in the longitude range corresponding to the void lobe in the fourth quadrant, Mège et al. (2021) found a relatively high occurrence of noise in the original spectral survey data which in many cases prevented an estimation of the radial velocity and hence of the kinematic distance. In any case, since the two void areas are oriented approximately along Galactocentric radial directions, their influence is distributed over a certain number of rings (and therefore attenuated).

The dip in the SFR density profile is followed by another local peak at around 5 kpc. A peak in this position was predicted by Krumholz & McKee (2005) as a consequence of the distribution of the molecular gas surface density, and was found also by Portinari & Chiosi (1999) and Chiappini et al. (2001), but at ~ 4 kpc. It should correspond to the so-called Molecular Ring (which is, more realistically, an effect of spiral arm arrangement; see Dobbs & Burkert 2012; Roman-Duval et al. 2016; Miville-Deschênes et al. 2017), but it does not mirror exactly the peak of source number distribution found by Elia et al. (2017) at $R_{\text{gal}} \simeq 6$ kpc. Finally, at larger distances, Σ_{SFR} definitely shows a systematic decrease.

This global behavior is qualitatively similar to those shown by Kennicutt & Evans (2012; starting from the data of

---

[19] To correctly compare this plot with Figure 5, it must be considered that in this case the SFR density is obtained by dividing by the ring area, proportional to R_{gal}^2, while in Figure 5 the denominator consists of a local area extending over $0.25 \, \text{kpc}^2$. Also notice that, as discussed in Section 2.2.1, the distribution in longitude of sources without a distance assignment shows a remarkable concentration at $0° \lesssim \ell \lesssim 20°$. Assigning the distance of the Galactic center to all of them would turn out in an even higher value for this peak.

Table 2
Star Formation Rate Estimates for the Central Molecular Zone

Method	Area Boundaries	SFR$_{CMZ}$ (lit.) ($M_\odot$ yr^{-1})	References	SFR$_{CMZ}$ (this Work) ($M_\odot$ yr^{-1})
YSO counts (Spitzer)	$|\ell| < 1°$, $|b| < 10'$	0.14	Yusef-Zadeh et al. (2009)	0.04 ± 0.02
Continuum emission at 60, 100 μm (IRAS)	$|\ell| < 3°$, $|b| < 1°$ [a]	0.12	Crocker et al. (2011)	0.12 ± 0.05
Continuum emission at 60, 100 μm (IRAS)	$|\ell| < 0.8°$, $|b| < 0.3°$	0.08	Crocker et al. (2011)	0.04 ± 0.02
YSO counts (Spitzer)	$|\ell| < 1.5°$, $|b| < 0.5°$	0.08	Immer et al. (2012)	0.08 ± 0.03
Ionization rate from radio free–free	$2.5° < \ell < 3.5°$, $|b| < 0.5°$	0.035	Longmore et al. (2013)	0.11 ± 0.04
Ionization rate from radio free–free	as above, but $|b| < 1°$ for $|\ell| < 1°$	0.06	Longmore et al. (2013)	0.12 ± 0.05
Continuum emission at 24 μm (Spitzer)	$|\ell| < 1°$, $|b| < 0.5°$	0.09 ± 0.02		
Continuum emission at 70 μm (Spitzer)	$|\ell| < 1°$, $|b| < 0.5°$	0.10 ± 0.02	Barnes et al. (2017) [b]	0.06 ± 0.02[c]
Cont. emission at 5.8–500 μm (Spitzer, Herschel)	$|\ell| < 1°$, $|b| < 0.5°$	0.09 ± 0.03		

Notes.
[a] Differently from other rectangular areas quoted in the table, this one has an elliptical shape with axes aligned along ℓ and b, and semiaxes of 3° and 1°, respectively.
[b] In Barnes et al. (2011), their Table 2, a further list of SFR$_{CMZ}$ estimates derived within the same area from monochromatic fluxes or bolometric luminosities available in the literature from 1998 to 2011 are quoted (see text). We omit them in this table for the sake of brevity.
[c] The three SFR$_{CMZ}$ estimates by Barnes et al. (2017) are derived within the same area in the sky through different methods; obviously, for the same area we can provide only one estimate.

Guesten & Mezger 1982) and Lee et al. (2016): an absolute maximum corresponding to the CMZ, followed by a local minimum and by another local peak at $R_{gal} = 1$ and 5 kpc, respectively, with a decreasing behavior at larger Galactocentric distances. This general behavior was successfully modeled by Evans et al. (2022) by taking into account (i) a dependence of the conversion factor from CO luminosity to cloud mass on metallicity (which in turn depends on R_{gal}), and (ii) a dependence of the star formation efficiency on the virial parameter. The envelope of the six models produced by Evans et al. (2022, their Figure 3) in the Σ_{SFR} versus R_{gal} diagram delimits a belt (with a vertical width of 1–2 dex) in which the curve observed by Lee et al. (2016) is contained. The latter being quite similar to ours in many points (Figure 6, top), a similar consistency is expected also for our data. In fact, our Σ_{SFR} curve is found, in turn, to be enclosed within the region occupied by the models of Evans et al. (2022), running closer to the top of it around the $R_{gal} \simeq 5$ kpc peak, and to the bottom of it at larger Galactocentric distances, in the range corresponding to the final decrease.

It is also important to compare the SFR profile found for the Milky Way with those of external galaxies, to examine if some macroscopic bias is introduced when observing the Galaxy from the inside, rather than as a whole from the outside. The SFR Galactocentric profile of the NGC 6946 galaxy obtained by Schruba et al. (2011) and adapted by Kennicutt & Evans (2012) shows, in turn, a qualitatively similar but flatter behavior. More recently, Logroño-García et al. (2019), using Hα emission, estimated for NGC 3994 and NGC 3995 SFR profiles which, although not quantitatively similar to that of the Milky Way, again broadly follow the same sequence of peaks and dips. Interestingly, a similar inner dip was also found by Lian et al. (2018) to be typical of local massive star-forming galaxies ($10.5 < \log(M/M_\odot) < 11$).

Returning to the SFR density profile of the Milky Way and to its decrease for $R_{gal} \gtrsim 5$ kpc, Misiriotis et al. (2006) found a good agreement between the radial profile of SFR density collected from the literature and their model of spatial distribution of dust, stars, and gas in the Milky Way, constrained through COBE/DIRBE data. Such model has a functional form:

$$\log(\Sigma_{SFR}/[M_\odot \text{ yr}^{-1} \text{ kpc}^{-2}]) = a\,R_{gal}/[\text{kpc}] + b, \quad (2)$$

with $a \sim -0.14$. Fitting the same relation to our data for $R_{gal} \geqslant 5$ kpc, we obtain $a = -0.28 \pm 0.01$ (Figure 6, top).

The linear fit in the same range of Galactocentric distance for the Guesten & Mezger (1982) has a much shallower slope ($a = -0.11 \pm 0.02$), while the more recent curve of Lee et al. (2016), which shows more scattering, has a slope consistent with ours: $a = -0.25 \pm 0.05$. Finally, in the NGC 6946 case the slope shows an intermediate behavior ($a = -0.20 \pm 0.01$).

The slope of -0.28 corresponds to an exponential scale length of 1.55 kpc, which is considerably shorter than those typically found for the stellar count profile in the Galactic thin disk, e.g., 2.15 kpc by Licquia & Newman (2015), 2.6 kpc by Bland-Hawthorn & Gerhard (2016, see also further references therein), and 2.2 kpc by Xiang et al. (2018). However, more recently, by using LAMOST Data Release 4 (Cui et al. 2012; Deng et al. 2012) and Gaia Data Release 2 (Gaia Collaboration et al. 2018; Lindegren et al. 2018), Yu et al. (2021) derived shorter scale lengths. In particular, they considered separately stellar populations characterized by different chemical abundances; the scale length that most closely approaches ours is that found for stars with solar-type abundances, 1.28 kpc (but for $R_{gal} > 8$ kpc).

In Figure 6, bottom, the behavior of the SFR profile as a function of R_{gal} is further analyzed by means of its cumulative. Although this curve is reminiscent of the SFR density profile shown in the top panel, it additionally accounts for the increasing area of the ring at increasing R_{gal}. For our data we notice three very evident changes of slope in the cumulative at around 4 (marked steepening), 7 (getting shallower), and 10 kpc (flattening), respectively. We find that the 50%, 90%, and 99% of total SFR are achieved at $R_{gal} = 5.8$, 9.2, and 13.4 kpc, respectively. This means that, according to our results, half of the Galactic SFR comes from within the Molecular Ring, and just 1% from the far outer Galaxy ($R_{gal} > 13.5$ kpc, according to the definition by Heyer et al. 1998).
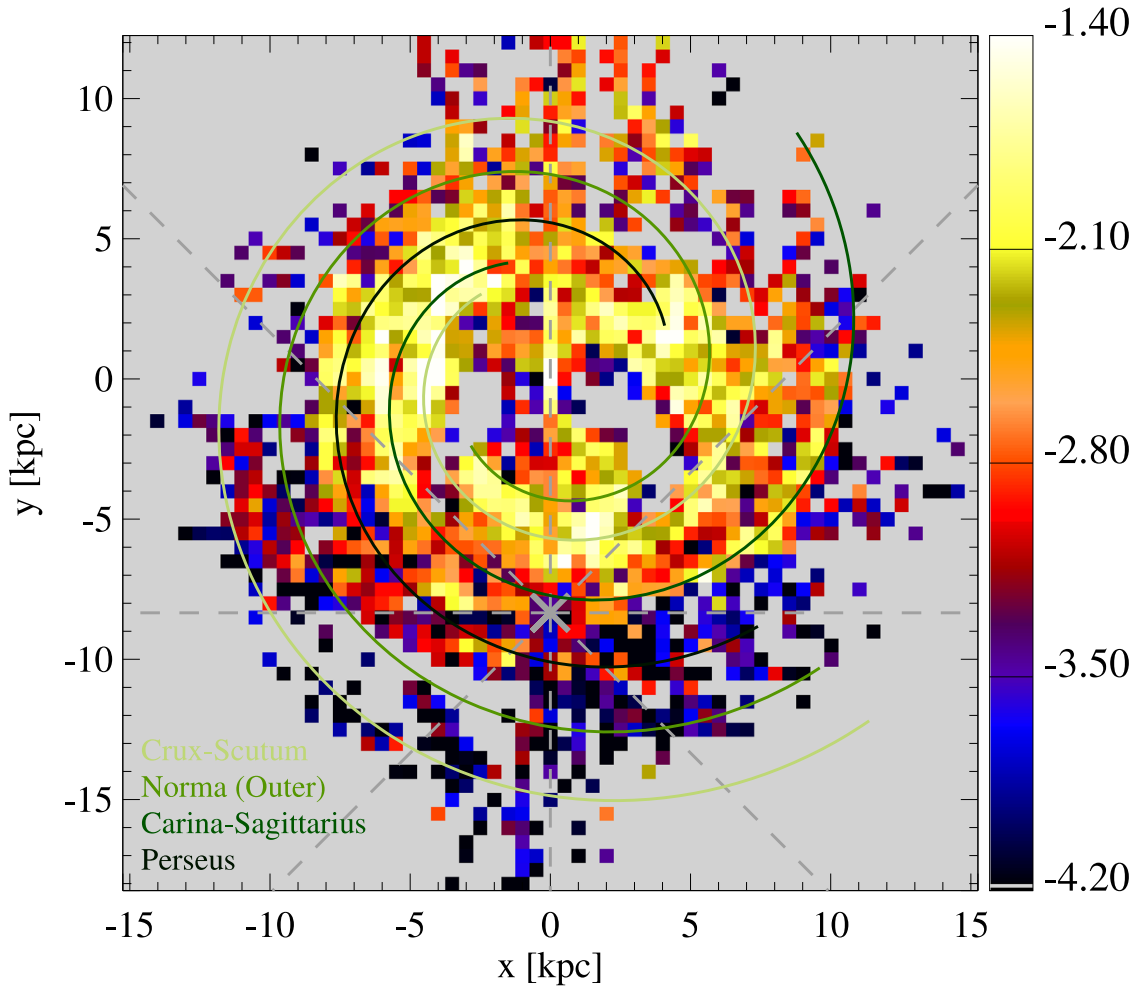
Figure 5. Map of the decimal logarithm of SFR density (divided by $M_\odot$ yr^{-1} kpc^{-2}), across the Galactic plane. The spatial bins are of 0.5×0.5 kpc^2, so that the absolute SFR inside each pixel can be obtained by exponentiating the displayed logarithm and then multiplying by a factor 4 kpc^2. The Galactic center is at the [0, 0] position, while the gray "X" symbol indicates the position of the Sun. Gray dashed lines mark Galactic octants. Four spiral arms according to the prescription of Hou et al. (2009) are overplotted with four different tones of green; the correspondence between arms and colors is explained in the legend at the bottom-left corner.

3.3. Testing the Kennicutt–Schmidt Relation

The SFR density profile computed in rings of R_{gal} and plotted in the top panel of Figure 6 can be also used for checking if the SFR in the Milky Way follows the KS law.

This is an empirical scaling relation (Schmidt 1959; Kennicutt 1998) generally found between SFR density, Σ_{SFR}, and mean gas (atomic + molecular) surface density, Σ_{gas}, in disk galaxies (the atomic and molecular gas density, $\Sigma_{H\,I}$ and Σ_{H_2}, respectively, can be also considered separately; see Bigiel et al. 2008; Kennicutt & Evans 2012). It is expressed by a power law such as

$$\Sigma_{SFR} \propto \Sigma_{gas}^n, \qquad (3)$$

with n generally falling in the range 1–2, depending on the tracer used and the linear scales considered. In particular, the "classic" slope of Kennicutt (1998) is $n = 1.40 \pm 0.15$, with Σ_{gas} expressed in units of $M_\odot$ pc^{-2}. Finally, in the literature descriptions of Σ_{SFR} as a power law of the single atomic ($\Sigma_{H\,I}$), or molecular component (Σ_{H_2}), respectively, can be also commonly found.

Whereas a vast literature is available about external galaxies following the KS relation (see, e.g., Kennicutt 1998;

Miettinen et al. 2017; Orr et al. 2018, and references therein), this has been poorly tested for the Milky Way, also due to well-understood intrinsic difficulties related to observing the Galaxy "from within."

The KS relation for a set of regions in the southern Milky Way was explored by Luna et al. (2006), who considered only Σ_{H_2} and found an exponent $n = 1.2 \pm 0.2$. Similarly, Sofue & Nakanishi (2017) found $n = 1.12 \pm 0.05$ for a set of (Σ_{SFR}, Σ_{H_2}) pairs obtained through binning the Galactic plane in 0.2×0.2 kpc^2 boxes. No clear correlation was found, instead, between Σ_{SFR} and both $\Sigma_{H\,I}$ and Σ_{gas}. A steeper slope (3.7 ± 1.6), again considering only Σ_{H_2}, was found by Gutermuth et al. (2011). However, this value was based only on the analysis of a small sample of nearby star-forming regions, which are not necessarily representative of the entire Galaxy.

Since in our case the available data set includes the entire Galactic plane, the approach we follow here is to plot the (Σ_{SFR}, Σ_{H_2}) pairs azimuthally averaged in bins of Galacto-centric radius (i.e., rings). This was done, for example, in Boissier et al. (2003), who found that the KS relation is satisfied in the range $4 \leqslant R_{gal} \leqslant 15$ kpc with a slope of 2.06, and in Misiriotis et al. (2006), who obtained a slope of 2.18 across the entire range of R_{gal}.
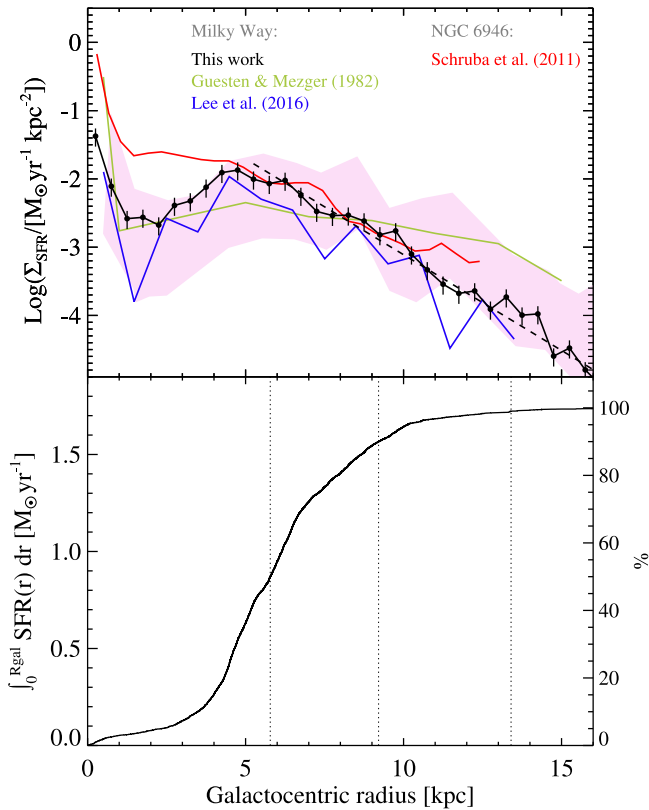
Figure 6. Top: star formation rate (SFR) density profile estimated from the Hi-GAL observations in 0.5 kpc wide concentric rings around the Galactic center, shown in black filled circles. Fitting the relation in Equation (2) to the portion at $R_{gal} \geqslant 5$ kpc gives $a = -0.28 \pm 0.01$ and $b = -0.30 \pm 0.16$. The fit is plotted as a black dashed line. The green line shows the results of the visible-band observations considered in Guesten & Mezger (1982), rescaled by Kennicutt & Evans (2012) to the total SFR of $1.9\,M_{\odot}\,yr^{-1}$ reported in Chomiuk & Povich (2011). The blue line corresponds to the estimates obtained in Lee et al. (2016) by combining YSO near-IR photometry and cloud properties from millimeter-line observations. The red line shows the SFR profile of the galaxy NGC 6946, presented in Schruba et al. (2011) and adapted by Kennicutt & Evans (2012). The pink-shaded area is the region occupied by the models of Evans et al. (2022). Bottom: cumulative SFR profile as a function of the Galactocentric radius, also expressed as a percentage with respect to the total SFR (y-axis on the right-hand side). The vertical dotted lines indicate, from left to right, the Galactocentric radii corresponding to 50%, 90%, and 99% of the total SFR, respectively.

To do that, for the x-axis we use the molecular Σ_{H_2} averaged over Galactocentric bins of 1 kpc by Miville-Deschênes et al. (2017), starting from the CO survey assembled by Dame et al. (2001), and the atomic $\Sigma_{H I}$ from Nakanishi & Sofue (2016). Therefore, for consistency, we recalculated the SFR density in the same bins (which are twice wider than those used for Figure 6).[20]

In Figure 7 the log–log plot of Σ_{SFR} versus Σ_{H_2} is shown. Differently from the plots built with the atomic and total gas density (see Appendix B), a linear trend can be recognized here, except for points corresponding to the innermost radii. For this reason, in the estimation of the linear fit, following the indication of Boissier et al. (2003), we do not consider the points corresponding to three first Galactocentric rings ($R_{gal} \leqslant 3$ kpc). Notice that, as can be seen in the bottom panel of Figure 6, the fraction of SFR contained within this radius

---

[20] See Onodera et al. (2010) and Kruijssen & Longmore (2014) for detailed discussions of minimum scales to be preserved while binning, to avoid incomplete sampling and consequent break down of star formation relations.
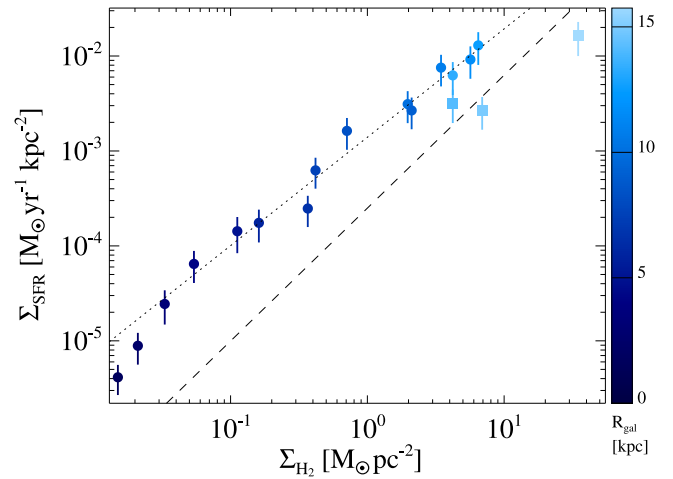

Figure 7. Star formation rate estimated from the Hi-GAL observations vs. the average molecular gas surface density (from Miville-Deschênes et al. 2017) in 1 kpc wide concentric rings around the Galactic center whose central radius is indicated by the colors. The bins corresponding to $R_{gal} \leqslant 3$ kpc and $R_{gal} > 3$ kpc are marked with square and circle symbols, respectively. The dotted and the dashed lines indicate the linear fit to the SFR estimates at $R_{gal} \geqslant 3$ kpc (with slope $n = 1.14 \pm 0.07$), and the KS relation ($\Sigma_{SFR} = 2.5 \times 10^{-4}\,\Sigma_{gas}^{1.4}$), respectively.

corresponds to only the 7% of the entire Milky Way SFR. From the fit to the remaining points, we obtain $n = 1.14 \pm 0.07$.

First of all, from the qualitative point of view, it is important to confirm that the largest part of the Milky Way disk follows a power-law behavior, testifying a direct and clear connection between the availability of molecular gas and the rate of its conversion into stars.

The slope n value we found appears in good agreement with those derived by Luna et al. (2006) and Sofue & Nakanishi (2017), while it is shallower than those found by Boissier et al. (2003) and Misiriotis et al. (2006). Furthermore, we note the agreement of our result with that obtained by Onodera et al. (2010) for the M33 galaxy ($n = 1.18 \pm 0.11$). The comparison with the classic slope of Kennicutt (1998), instead, makes little sense, since it refers to the total Σ_{gas}.

Actually, it is known that a variety of slopes is generally found for the KS relation (see, e.g., Kennicutt & Evans 2012, and references therein). Furthermore, it is not difficult to figure out how varying some assumptions made in calculating the plotted variables can produce a change of the slope (even though preserving the global power-law behavior). For example, surface densities were computed by Miville-Deschênes et al. (2017) by converting CO to H_2 by using the constant factor $X_{CO} = 10^{20}\,cm^{-2}\,(K\,km\,s^{-1})^{-1}$. However, if an increasing trend of X_{CO} at increasing R_{gal} was adopted (e.g., Nakanishi & Sofue 2006; Pineda et al. 2013), the plot in Figure 7 would get steeper (see also Boissier et al. 2003). Moreover, the masses used here as input for the SFR calculation were derived by Elia et al. (2021) by assuming a constant gas-to-dust ratio of 100. However, a possible increase of this ratio at increasing R_{gal} is suggested by Giannetti et al. (2017), and invoked by Elia et al. (2021) themselves to better explain the Galactocentric behavior of the surface density of Hi-GAL clumps. Taking into account such dependence would produce a flattening of our Σ_{SFR} versus Σ_{H_2} plot.
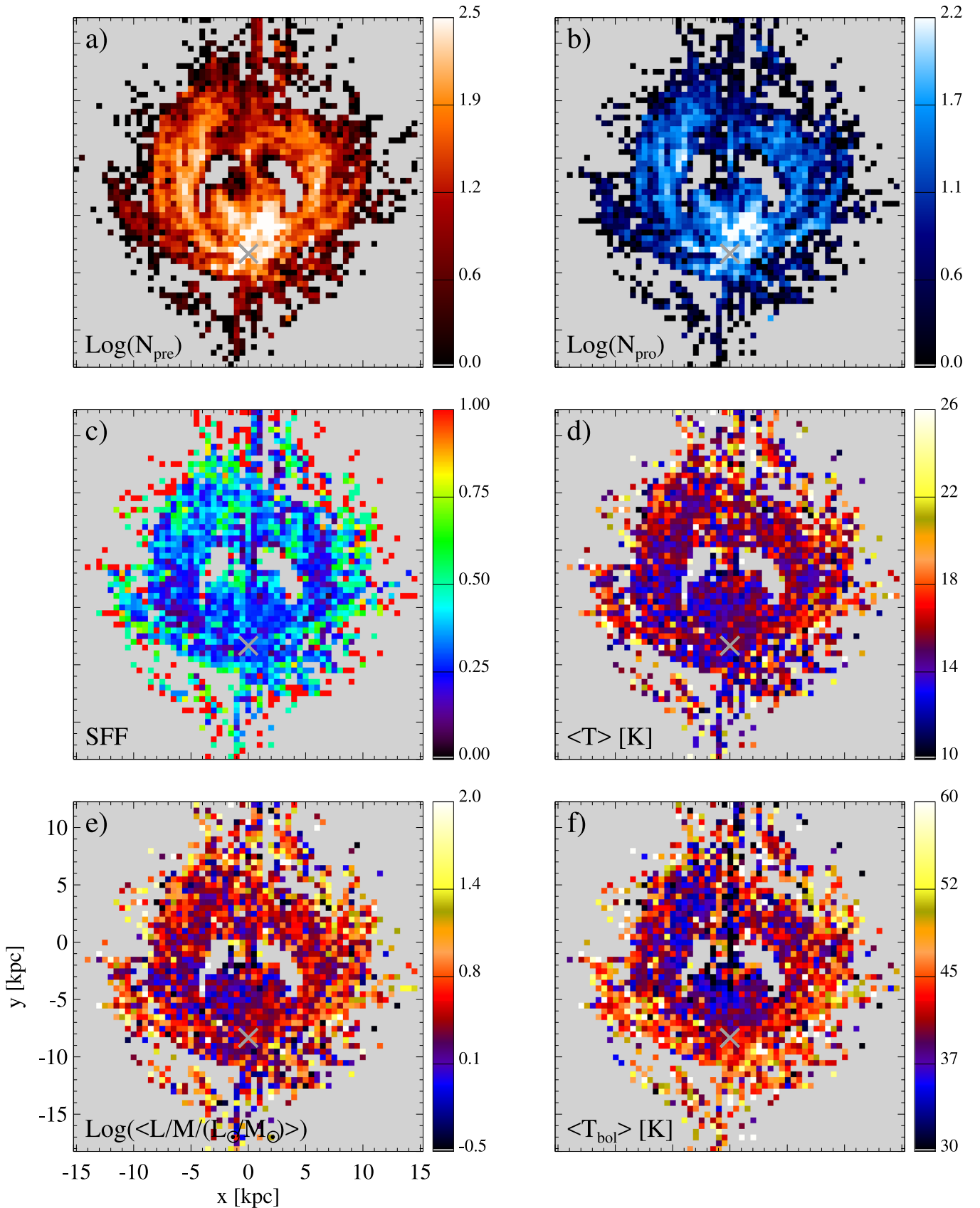
Figure 8. Face-on view of the Milky Way representing the following quantities derived (with the same spatial binning used for Figure 5) from the Hi-GAL observations: (a) logarithm of number of pre-stellar Hi-GAL clumps per bin, N_{pre}; (b) logarithm of number of protostellar Hi-GAL clumps per bin, N_{pro}; (c) star formation fraction, SFF; (d) median temperature (from modified blackbody fit) of protostellar clumps, $\langle T \rangle$; (e) median logarithm of luminosity-to-mass ratio normalized to the solar values, $\langle (L/M)/(L_{\odot}/M_{\odot}) \rangle$; (f) median bolometric temperature of protostellar clumps, $\langle T_{bol} \rangle$. In each panel, the [0, 0] position corresponds to the Galactic center position, and the gray "X" symbol indicates the position of the Sun.
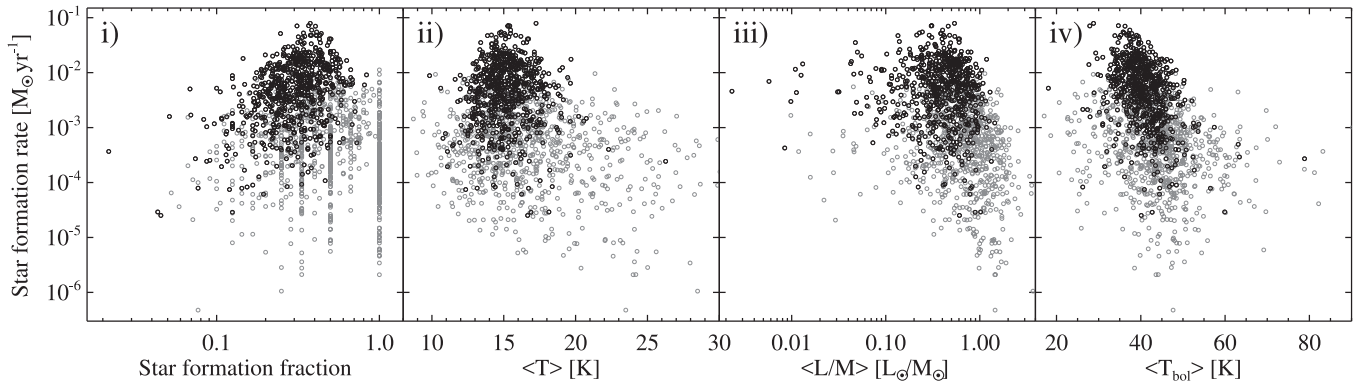
Figure 9. Star formation rate, evaluated in bins of 0.5 kpc in the $[x, y]$ plane, as a function of star formation fraction (i), and medians of temperature (ii), L/M ratio (iii), and bolometric temperature (iv) of protostellar clumps, respectively, all calculated in the same spatial bins. In this respect, they represent a pixel-to-pixel plot of Figure 5 vs. panels (c), (d), (e), and (f) of Figure 8, respectively. Gray symbols correspond to bins with $N_{pro} + N_{pre} < 20$, considered statistically poor. In the leftmost panel, several of them give rise to vertical features, corresponding to recurring values like $N_{pro}/(N_{pro} + N_{pre}) = \frac{1}{1}, \frac{1}{2}, \frac{1}{3}, \frac{1}{4}$, etc.

3.4. Face-on View of the Milky Way's Star Formation Rate

Mapping the SFR in the Galactic plane, as in Figure 5, offers the chance of comparing the local values of this observable with those of other quantities that can be mapped starting from the Hi-GAL clump distribution in the plane.

In our estimates, the SFR is the sum of the contributions from each protostellar clump, which is a function of its mass. In this respect, the spatial distribution of SFR in bins of $[x, y]$ coordinates mirrors that of the total mass of protostellar clumps in those bins. This total mass, in turn, does not necessarily depend on the number of protostellar clumps, N_{pro}, found in each bin (shown in Figure 8(b)),[21] and does not depend at all on the number of pre-stellar clumps, N_{pre} (shown in Figure 8(a)). These two quantities were combined together by Ragan et al. (2016) to obtain the star formation fraction (hereafter SFF), defined as the ratio $N_{pro}/(N_{pre} + N_{pro})$. The relative populations of these two classes depend on their corresponding lifetimes, which in turn depend on the mass (Motte et al. 2010; Urquhart et al. 2014; Elia et al. 2021). In this respect, the local SFF is related not only to the overall evolutionary state of clumps in a given region, but also, indirectly, to their mass spectrum. Using Hi-GAL data, Ragan et al. (2016) highlighted a decreasing behavior of SFF as a function of the Galactocentric radius over the 3.1 kpc $< R_{gal} < 8.6$ kpc range. This was confirmed by Elia et al. (2021), who however found a more scattered behavior just outside this range. This 1D description of the SFF is further developed here in the 2D mapping shown in the panel (c) of Figure 8, in which we can recognize the aforementioned decrease of this quantity at intermediate Galactocentric radii as a blueish ring-like area.

It makes sense to compare here the maps of SFR and SFF, since on the one hand they have no direct link a priori, and on the other hand this allows us to check whether locally the SFR is somehow correlated to the average evolutionary stage of the region. A bin-to-bin comparison between SFR and SFF is

shown in panel (i) of Figure 9. Apparently, no correlation emerges from the plot, except for the fact that a small number of bins with very low SFF ($\ll 1$) also exhibit relatively low SFR values.

As a further check of the absence of a trend with the average evolutionary stage of clumps in different parts of the disk, we also investigate the trend of the SFR versus the medians of meaningful evolutionary indicators for protostellar clumps, such as modified blackbody temperature T, bolometric luminosity over mass ratio L/M, and bolometric temperature T_{bol} (Cesaroni et al. 2015; Elia et al. 2017, 2021). Median values were evaluated for them in the same spatial bins of Figure 5, and displayed in Figure 8, panels (d), (e), and (f), respectively.

For the median temperature and L/M ratio of protostellar clumps, Elia et al. (2021) did not find relevant variations in the 1D profile as a function of R_{gal}, apart from an increase in the far outer Galaxy, but supported by poor statistics. On the contrary, the trend found for median T_{bol} is to slightly raise at increasing R_{gal}. This is what can be seen also in the 2D view provided in Figure 8. Therefore, the bin-to-bin comparison of quantities nearly constant with R_{gal} such as T and L_{bol}/M and an observable with a more complex spatial pattern (SFR) is expected to show no correlation between the two, as confirmed by Figure 9, panels (ii) and (iii). A mild indication seems to be provided by bins with poor statistics (i.e., containing less than 20 clumps, so an even smaller number of protostellar ones), generally corresponding to large R_{gal}, for which a higher L/M but a small SFR (due to deficit of clumps) can be found. A similar, but clearer, behavior can be seen also considering the median T_{bol} (panel (iv)), essentially due to the increase of this observable with R_{gal}.

The large degree of scatter between the local SFR and median evolutionary indicators suggests that while the SFR, as it is calculated here, essentially depends on the local availability of mass, it is quite insensitive to the average evolutionary stage of clumps. In fact, it increases with the number of protostellar clumps and with their masses. Therefore, massive star-forming regions surely provide a relevant contribution to the SFR of the Milky Way, however this does not seem to depend—once their mass is given—on an earlier or later mean evolutionary stage. This confirms the result found by Komugi et al. (2018) for M33, namely the fact that the SFR is clearly correlated with the cloud density, in a somewhat
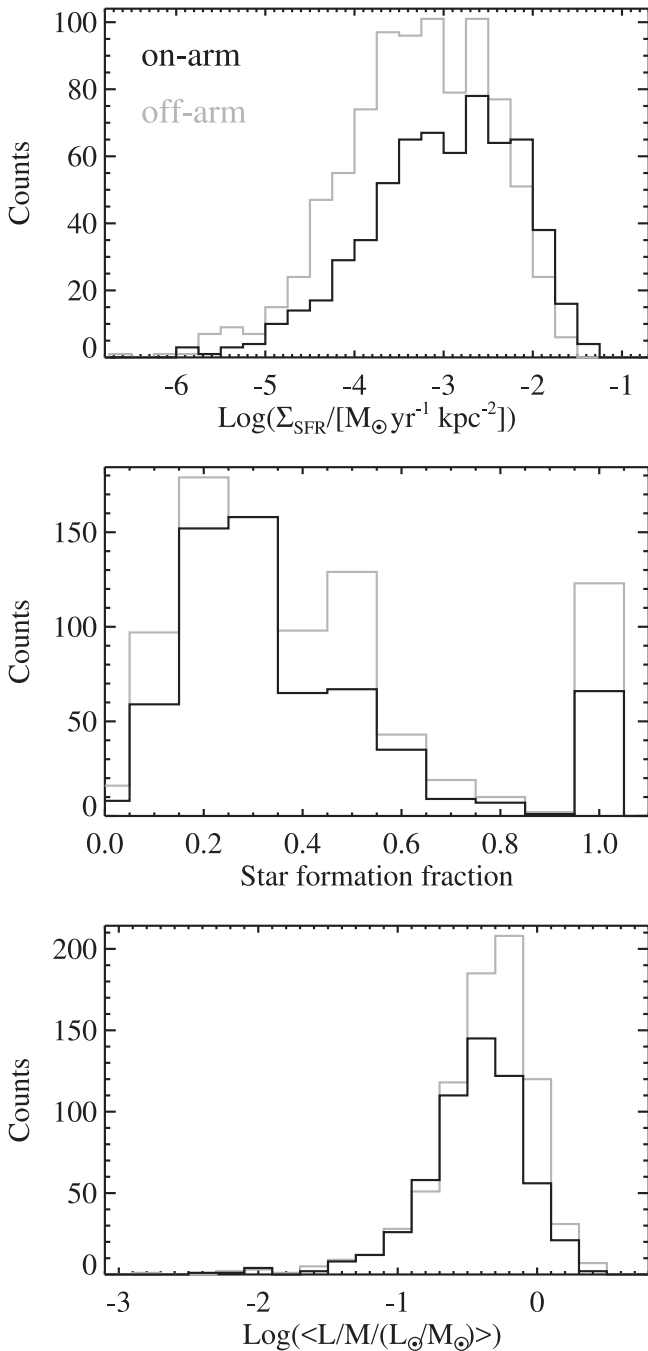
---

[21] Spatial distributions in panels (a) and (b) clearly appear asymmetric because at shorter heliocentric distances a larger number of sources (having relatively smaller physical sizes and masses) is detected. Conversely, at higher distances sources tend to appear blended in physically larger structures (Section 2.1). Since the SFR depends on the available mass (Section 2.2), the final appearance of the SFR density map in Figure 5 appears much more symmetric than that of source counts. Moreover, the selection bias with distance has to be taken into account; this is done in Appendix A.

Figure 10. Top: histograms of logarithm of SFR density for pixels of the map in Figure 5, classified as on-arm (black) and off-arm (gray), based on the fact that their minimum distance from at least one of the spiral arms displayed in Figure 5 is shorter or longer than 0.5 kpc, respectively. Middle: the same as in the top panel, but for pixels of the map of SFF in Figure 8, panel (c). Bottom: the same as in the previous panels, but for pixels of the map of $\langle L_{bol}/M \rangle$ in Figure 8, panel (e).

extended meaning of the KS relation, but not with the evolutionary stage.

3.5. Star Formation Rate and Spiral Arm Locations

In several portions of the spatial distribution of SFR density Σ_{SFR} in the Galactic plane shown in Figure 5 it is possible to recognize stretches of spiral arm features, similarly to what has been observed in external galaxies (Rebolledo et al. 2015; Elagali et al. 2019; Yu et al. 2021).

The SFR arm-like features are not much different from the pattern visible also in the distribution of protostellar clumps (Figure 8, panel (b)), i.e., the elements from which the SFR is computed. However, as already discussed in Elia et al. (2017, 2021), a relevant amount of clumps with "inter-arm" distances is also found, due to a large spread in velocities detected along many lines of sight of spectral surveys (Mège et al. 2021). Additionally, each different analytic spiral arm prescription available in the literature is able to successfully reproduce the observations over wide ranges of longitude, but can fail to fit observed arm-like features along other directions.

In Figure 5 we show, as an example, the four-arm prescription by Hou et al. (2009). It appears in good agreement with enhancements of our SFR density map along a significant portion of the Perseus Arm; a good agreement is also found for the Norma and Carina–Sagittarius arms in the third quadrant, and for the Carina–Sagittarius and Crux–Scutum arms in the first octant of the fourth quadrant, respectively. Nevertheless, there are other regions with high SFR density but not directly intersected by one of the displayed arms. All these aspects are mirrored in the distribution of the Σ_{SFR} values in Figure 5, if pixels closer than 0.5 kpc from whatever spiral arm candidate plotted in the figure are considered separately from the remaining ones (Figure 10, top). The distribution of the "on-arm" pixels is visibly more left-skewed than the one of the "off-arm" pixels. In short, we observe a sufficiently clear spiral arm structure in the SFR spatial distribution, which elects spiral arms as preferential (although not unique) places for star formation activity in the Galaxy.

A similar spiral arm-like structure, on the contrary, is not seen in Figure 8 in the distributions of both SFF (panel (c)) and median evolutionary indicators as T (d), L_{bol}/M (e), and T_{bol} (f). Figure 10, middle, contains a comparison between the on-arm and off-arm distributions of SFF. These two distributions appear to be much less distinguishable than in the case of Σ_{SFR} (top panel). A similar behavior can be also seen for $\langle L_{bol}/M \rangle$ (Figure 10, middle), taken as an example for the three considered evolutionary indicators.

These considerations reinforce the conclusions of Ragan et al. (2016) and Elia et al. (2021) about the role of spiral arms, i.e., that no significant differences in the mean evolutionary stage of star formation between spiral arms and inter-arm regions are found. The main difference between these two regions seems rather to consist in the larger amount of material available for star formation in the former than in the latter (see also Moore et al. 2012).

4. Summary

We used the information contained in the catalog of Hi-GAL clump physical properties to obtain a self-consistent estimate of the Milky Way SFR. The main points to be summarized are as follows:

1. We extrapolated from the algorithm proposed by Veneziani et al. (2013, 2017) an operative analytic prescription to obtain the contribution to the SFR from the mass of each FIR clump: $SFR_{clump} = 5.6 \times 10^{-7} \, (M_{clump}/M_\odot)^{0.74} \, M_\odot \, yr^{-1}$.
2. Considering all clumps classified as protostellar (i.e., star-forming) in the catalog and provided with a heliocentric distance, we obtain $SFR = 1.7 \pm 0.6 \, M_\odot \, yr^{-1}$.
3. If we also take into account the contribution from the protostellar clumps without distance assignment, we

estimate an additional contribution of $0.22\,M_\odot\,\mathrm{yr}^{-1}$ to the global SFR, assuming that their distances follow the same distribution as the sources with known locations. This would lead to a final SFR $= 2.0 \pm 0.7\,M_\odot\,\mathrm{yr}^{-1}$. Also simulating the extreme case consisting in placing all those sources at $d = 13\,\mathrm{kpc}$, the corrective term would not surpass $0.57\,M_\odot\,\mathrm{yr}^{-1}$.

4. The profile of SFR surface density as a function of the Galactocentric radius R_{gal} is qualitatively similar to other results in the literature for the Milky Way and NGC 6946, and is consistent with most recent models (Evans et al. 2022). The absolute maximum is found in correspondence of the CMZ, and another local peak is found around $R_{\mathrm{gal}} = 5\,\mathrm{kpc}$, after which the logarithm of SFR density linearly decreases at increasing R_{gal}, with slope -0.28.

5. Studying the cumulative of the SFR as a function of the Galactocentric radius, we find that 50% of the entire Milky Way SFR comes from within the so-called Molecular Ring, and 84% from within the solar circle (inner Galaxy, $R_{\mathrm{gal}} < 8.34$ kpc). The outer Galaxy is therefore responsible for 16% of total SFR and, in particular, the far outer Galaxy ($R_{\mathrm{gal}} > 13.5$ kpc) for 1%.

6. The relation between SFR density and the molecular gas surface density Galactocentric profiles follows, for $R_{\mathrm{gal}} > 3$ kpc (containing the 93% of the entire Galactic SFR), a KS law behavior, with slope $n = 1.14 \pm 0.07$.

7. We find no significant trend relating the maps of SFR and those of the observables considered indicative of the mean local evolutionary stage of clumps. We conclude that the local SFR is determined by the amount of available mass rather than by the clump evolutionary stage.

8. In the distribution of SFR across the Galactic plane, arm-like enhancements emerge over wide ranges of longitude. These enhancements are not seen in maps of the clump evolutionary indicators, suggesting that they are produced by source crowding within the arms.

Appendix A
Evaluating the Completeness of the Total Star Formation Rate Estimate for the Milky Way

Here we provide an estimate of the validity of the total SFR derived for the Milky Way in Section 2.2 in the light of possible incompleteness of the Hi-GAL catalog for large heliocentric distances.

Elia et al. (2017) showed how the mass completeness limit for Hi-GAL, based on the 350 μm band flux, varies with source temperature and distance. For $T = 16$ K, similar to the median temperature for Hi-GAL star-forming clumps (Elia et al. 2021), a distance $d = 10$ kpc, and a typical flux completeness limit of 5 Jy for the inner Galaxy (Molinari et al. 2016), the mass completeness limit amounts to $\sim 90\,M_\odot$. One can therefore
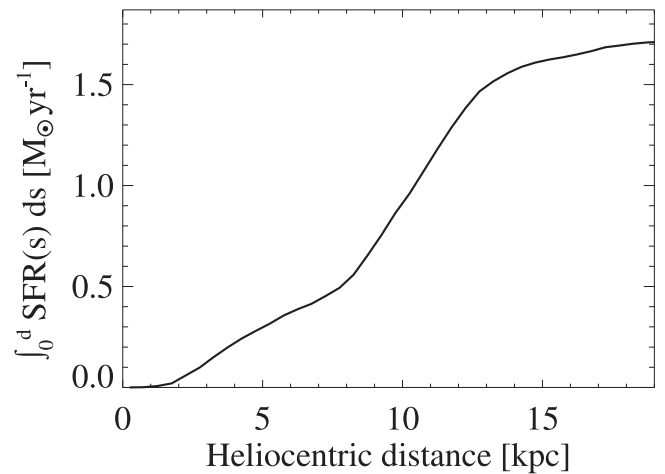

Figure A1. Cumulative SFR profile as a function of the heliocentric distance. Since the distance d appears as an upper limit of integration, here the integration variable is called s.

expect a shortage of detected clumps with mass lower than that, ignored in the SFR calculation. Here we give a quantitative discussion of this possible effect.

First, we compute the cumulative SFR as a function of the distance. In Figure A1 a sharp change from a steeply positive to an almost horizontal slope is seen around $d = 12$ kpc. The same can be affirmed, but in terms of source number, noting that around the same distance a decreasing trend is seen to start also in Figure 2. Such a change of slope can, in principle, be a combination of the true distribution of the SFR density in the plane and the selection effect due to the distance we want to quantify. In the Hi-GAL catalog distances $d > 12$ kpc are achieved by sources in the first and fourth quadrants[22] and the total SFR due to such sources is $0.45\,M_\odot\,\mathrm{yr}^{-1}$.

Second, we evaluated the SFR from the symmetrical region on the opposite side of the Milky Way, i.e., we considered clumps (essentially located in the second and third quadrants) lying outside the circle centered on the symmetric point of the Sun with respect to the Galactic center ($[x, y] = [0, +8.34]$ kpc) and with a radius of 12 kpc. The SFR from this area amounts to $0.60\,M_\odot\,\mathrm{yr}^{-1}$, so that, in the rough assumption of a circular symmetry for the "true" SFR distribution in the $[x, y]$ plane, the "missing SFR" due to incompleteness is comparable to the difference in SFRs measured from the two zones, namely $0.15\,M_\odot\,\mathrm{yr}^{-1}$. The extent of this correction shows that the effect of the catalog incompleteness is not very strong, although not negligible: it should be added as a further term to the total estimate of $1.7\,M_\odot\,\mathrm{yr}^{-1}$ based on clumps provided with a distance estimate (Section 2.2), then representing a 8% correction to it.

To evaluate an analogous additional term for the SFR of $2.0\,M_\odot\,\mathrm{yr}^{-1}$, estimated by involving also clumps with no distances (Section 2.2.1) is more complicated, because the distribution itself of known distances is involved in the calculation. However, assuming a 8% correction also in this case, the total Milky Way SFR would amount to $2.13\,M_\odot\,\mathrm{yr}^{-1}$.

---

[22] Notice that, since the relation between Galactocentric radius and heliocentric distance is $R_{\mathrm{GC}} = \sqrt{R_0^2 + d^2 + 2R_0 d \cos \ell}$, sources placed at a same distance span a variety of Galactic locations, with the minimum R_{GC} achieved for $\ell = 0°$.

Appendix B
Testing the Kennicutt–Schmidt Relation with Atomic Gas

To complete the discussion about the SFR versus gas density relation contained in Section 3.3, here we show the plots of Σ_{SFR} versus $\Sigma_{H\,I}$ (Figure B1, left) and $\Sigma_{gas} = \Sigma_{H\,I} + \Sigma_{H_2}$ (right), respectively, obtained using the Galactocentric profile of H I surface density of Nakanishi & Sofue (2016, their Figure 4).

Comparing such a profile with that of Σ_{SFR}, peaks for these two quantities are seen at very different values of R_{GC} (at $\sim$10 and $\sim$5 kpc, respectively), preventing a power-law relation between the two. Furthermore, for $R_{GC} \lesssim 20$ kpc, $\Sigma_{H\,I}$ varies only within

one order of magnitude (namely between $\sim$1 and $10\,M_{\odot}\,pc^{-2}$), so that the plot assumes an almost vertical appearance, as already highlighted by Sofue & Nakanishi (2017) and Bacchini et al. (2019). In this last work, in particular, it was shown how a power-law behavior is recovered if the atomic+molecular gas volume density instead of the surface density is considered, which implies taking into account the increasing Galactic disk scale height at increasing R_{GC}.

Similar considerations can be formulated if one considers also the total gas surface density, which, as it can be seen in Miville-Deschênes et al. (2017), is dominated by the atomic component at $R_{GC} \gtrsim 7$ kpc.
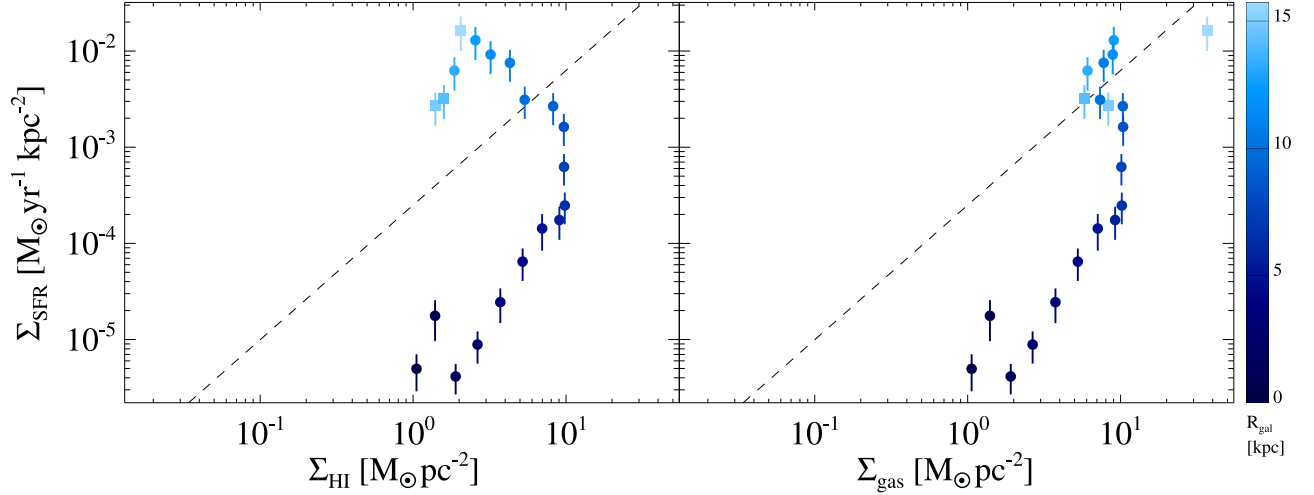

Figure B1. Left: the same as in Figure 7, but with atomic gas surface density on the *x*-axis (from Nakanishi & Sofue 2016), instead of the molecular one. The KS relation is also plotted as a dashed line. Right: the same as in Figure 7 and in the left panel of this figure, but with total gas surface density on the *x*-axis. In both panels the *x*-axis range has been kept identical to that of Figure 7, to facilitate comparison.

Elia et al.

ORCID iDs

D. Elia ⓘ https://orcid.org/0000-0002-9120-5890
S. Molinari ⓘ https://orcid.org/0000-0002-9826-7525
E. Schisano ⓘ https://orcid.org/0000-0003-1560-3958
J. D. Soler ⓘ https://orcid.org/0000-0002-0294-4465
M. Merello ⓘ https://orcid.org/0000-0003-0709-708X
D. Russeil ⓘ https://orcid.org/0000-0001-5400-7214
A. Zavagno ⓘ https://orcid.org/0000-0001-9509-7316
A. Noriega-Crespo ⓘ https://orcid.org/0000-0002-6296-8960
L. Olmi ⓘ https://orcid.org/0000-0002-1162-7947
M. Benedettini ⓘ https://orcid.org/0000-0002-3597-7263
P. Hennebelle ⓘ https://orcid.org/0000-0002-0472-7202
R. S. Klessen ⓘ https://orcid.org/0000-0002-0560-3172
S. Leurini ⓘ https://orcid.org/0000-0003-1014-3390
R. Paladini ⓘ https://orcid.org/0000-0002-5158-243X
S. Pezzuto ⓘ https://orcid.org/0000-0001-7852-1971
A. Traficante ⓘ https://orcid.org/0000-0003-1665-6402
D. J. Eden ⓘ https://orcid.org/0000-0002-5881-3229
P. G. Martin ⓘ https://orcid.org/0000-0002-5236-3896
M. Sormani ⓘ https://orcid.org/0000-0001-6113-6241
A. Coletta ⓘ https://orcid.org/0000-0001-8239-8304
T. Colman ⓘ https://orcid.org/0000-0002-2636-4377
R. Plume ⓘ https://orcid.org/0000-0002-6482-8945
Y. Maruccia ⓘ https://orcid.org/0000-0003-1975-6310
C. Mininni ⓘ https://orcid.org/0000-0002-2974-4703
S. J. Liu ⓘ https://orcid.org/0000-0001-7680-2139

References

André, P., Men'shchikov, A., Bontemps, S., et al. 2010, A&A, 518, L102
Bacchini, C., Fraternali, F., Pezzulli, G., et al. 2019, A&A, 632, A127
Baldeschi, A., Elia, D., Molinari, S., et al. 2017a, MNRAS, 466, 3682
Baldeschi, A., Molinari, S., Elia, D., Pezzuto, S., & Schisano, E. 2017b, MNRAS, 472, 1778
Barnes, A. T., Longmore, S. N., Battersby, C., et al. 2017, MNRAS, 469, 2263
Barnes, P. J., Yonekura, Y., Fukui, Y., et al. 2011, ApJS, 196, 12
Bennett, C. L., Fixsen, D. J., Hinshaw, G., et al. 1994, ApJ, 434, 587
Bergin, E. A., & Tafalla, M. 2007, ARA&A, 45, 339
Bigiel, F., Leroy, A., Walter, F., et al. 2008, AJ, 136, 2846
Binney, J., Gerhard, O. E., Stark, A. A., Bally, J., & Uchida, K. I. 1991, MNRAS, 252, 210
Bland-Hawthorn, J., & Gerhard, O. 2016, ARA&A, 54, 529
Boardman, N., Zasowski, G., Newman, J. A., et al. 2020, MNRAS, 498, 4943
Boissier, S., Prantzos, N., Boselli, A., & Gavazzi, G. 2003, MNRAS, 346, 1215
Cesaroni, R., Pestalozzi, M., Beltrán, M. T., et al. 2015, A&A, 579, A71
Chiappini, C., Matteucci, F., & Romano, D. 2001, ApJ, 554, 1044
Chomiuk, L., & Povich, M. S. 2011, AJ, 142, 197
Crocker, R. M., Jones, D. I., Aharonian, F., et al. 2011, MNRAS, 413, 763
Cui, X.-Q., Zhao, Y.-H., Chu, Y.-Q., et al. 2012, RAA, 12, 1197
Dame, T. M., Hartmann, D., & Thaddeus, P. 2001, ApJ, 547, 792
Davies, B., Hoare, M. G., Lumsden, S. L., et al. 2011, MNRAS, 416, 972
Deng, L.-C., Newberg, H. J., Liu, C., et al. 2012, RAA, 12, 735
Diehl, R., Halloin, H., Kretschmer, K., et al. 2006, Natur, 439, 45
Dobbs, C. L., & Burkert, A. 2012, MNRAS, 421, 2940
Dunham, M. M., Crapsi, A., Evans, N. J., II, et al. 2008, ApJS, 179, 249
Elagali, A., Staveley-Smith, L., Rhee, J., et al. 2019, MNRAS, 487, 2797
Elia, D., Merello, M., Molinari, S., et al. 2021, MNRAS, 504, 2742
Elia, D., Molinari, S., Fukui, Y., et al. 2013, ApJ, 772, 45
Elia, D., Molinari, S., Schisano, E., et al. 2017, MNRAS, 471, 100
Ellsworth-Bowers, T. P., Rosolowsky, E., Glenn, J., et al. 2015, ApJ, 799, 29
Evans, N. J., Kim, J.-G., & Ostriker, E. C. 2022, ApJL, 929, L18
Evans, N. J. I., Heyer, M., Miville-Deschênes, M.-A., Nguyen-Luong, Q., & Merello, M. 2021, ApJ, 920, 126
Fraser-McKelvie, A., Merrifield, M., & Aragón-Salamanca, A. 2019, MNRAS, 489, 5030
Gaia Collaboration, Brown, A. G. A., Vallenari, A., et al. 2018, A&A, 616, A1
Giannetti, A., Leurini, S., König, C., et al. 2017, A&A, 606, L12
Giannini, T., Elia, D., Lorenzetti, D., et al. 2012, A&A, 539, A156
Griffin, M. J., Abergel, A., Abreu, A., et al. 2010, A&A, 518, L3
Guesten, R., & Mezger, P. G. 1982, VA, 26, 159

Gutermuth, R. A., Pipher, J. L., Megeath, S. T., et al. 2011, ApJ, 739, 84
Heyer, M. H., Brunt, C., Snell, R. L., et al. 1998, ApJS, 115, 241
Hou, L. G., Han, J. L., & Shi, W. B. 2009, A&A, 499, 473
Immer, K., Schuller, F., Omont, A., & Menten, K. M. 2012, A&A, 537, A121
Jackson, J. M., Contreras, Y., Rathborne, J. M., et al. 2018, ApJ, 869, 102
Kennicutt, R. C., & Evans, N. J. 2012, ARA&A, 50, 531
Kennicutt, R. C., Jr. 1998, ApJ, 498, 541
Kennicutt, R. C., Jr., Hao, C.-N., Calzetti, D., et al. 2009, ApJ, 703, 1672
Koepferl, C. M., Robitaille, T. P., Morales, E. F. E., & Johnston, K. G. 2015, ApJ, 799, 53
Komugi, S., Miura, R. E., Kuno, N., & Tosaki, T. 2018, PASJ, 70, 48
Kroupa, P., & Weidner, C. 2003, ApJ, 598, 1076
Kruijssen, J. M. D., & Longmore, S. N. 2014, MNRAS, 439, 3239
Krumholz, M. R. 2014, PhR, 539, 49
Krumholz, M. R., & McKee, C. F. 2005, ApJ, 630, 250
Lada, C. J., Lombardi, M., & Alves, J. F. 2010, ApJ, 724, 687
Larson, R. B. 1981, MNRAS, 194, 809
Lee, E. J., Miville-Deschênes, M.-A., & Murray, N. W. 2016, ApJ, 833, 229
Li, Y., Calzetti, D., Kennicutt, R. C., et al. 2010, ApJ, 725, 677
Li, Z., Gerhard, O., Shen, J., Portail, M., & Wegg, C. 2016, ApJ, 824, 13
Lian, J., Thomas, D., Maraston, C., et al. 2018, MNRAS, 476, 3883
Licquia, T. C., & Newman, J. A. 2015, ApJ, 806, 96
Lindegren, L., Hernández, J., Bombrun, A., et al. 2018, A&A, 616, A2
Logroño-García, R., Vilella-Rojo, G., López-Sanjuan, C., et al. 2019, A&A, 622, A180
Longmore, S. N., Bally, J., Testi, L., et al. 2013, MNRAS, 429, 987
Luna, A., Bronfman, L., Carrasco, L., & May, J. 2006, ApJ, 641, 938
McKee, C. F., & Ostriker, E. C. 2007, ARA&A, 45, 565
McKee, C. F., & Williams, J. P. 1997, ApJ, 476, 144
Mège, P., Russeil, D., Zavagno, A., et al. 2021, A&A, 646, A74
Mezger, P. G. 1987, in Starbursts and Galaxy Evolution, ed. T. X. Thuan, T. Montmerle, & J. Tran Thanh van (Gif-sur-Yvette: Editions Frontieres), 3
Miettinen, O., Delvecchio, I., Smolčić, V., et al. 2017, A&A, 602, L9
Misiriotis, A., Xilouris, E. M., Papamastorakis, J., Boumis, P., & Goudis, C. D. 2006, A&A, 459, 113
Miville-Deschênes, M.-A., Murray, N., & Lee, E. J. 2017, ApJ, 834, 57
Molinari, S., Pezzuto, S., Cesaroni, R., et al. 2008, A&A, 481, 345
Molinari, S., Schisano, E., Elia, D., et al. 2016, A&A, 591, A149
Molinari, S., Schisano, E., Faustini, F., et al. 2011, A&A, 530, A133
Molinari, S., Swinyard, B., Bally, J., et al. 2010, PASP, 122, 314
Moore, T. J. T., Urquhart, J. S., Morgan, L. K., & Thompson, M. A. 2012, MNRAS, 426, 701
Motte, F., Zavagno, A., Bontemps, S., et al. 2010, A&A, 518, L77
Murray, N., & Rahman, M. 2010, ApJ, 709, 424
Mutch, S. J., Croton, D. J., & Poole, G. B. 2011, ApJ, 736, 84
Nakanishi, H., & Sofue, Y. 2006, PASJ, 58, 847
Nakanishi, H., & Sofue, Y. 2016, PASJ, 68, 5
Noriega-Crespo, A. 2013, in Cosmic Rays in Star-forming Environments, ed. D. F. Torres & O. Reimer (Berlin: Springer), 29
Onodera, S., Kuno, N., Tosaki, T., et al. 2010, ApJL, 722, L127
Orr, M. E., Hayward, C. C., Hopkins, P. F., et al. 2018, MNRAS, 478, 3653
Pilbratt, G. L., Riedinger, J. R., Passvogel, T., et al. 2010, A&A, 518, L1
Pineda, J. L., Langer, W. D., Velusamy, T., & Goldsmith, P. F. 2013, A&A, 554, A103
Poglitsch, A., Waelkens, C., Geis, N., et al. 2010, A&A, 518, L2
Portinari, L., & Chiosi, C. 1999, A&A, 350, 827
Ragan, S. E., Moore, T. J. T., Eden, D. J., et al. 2016, MNRAS, 462, 3123
Rebolledo, D., Wong, T., Xue, R., et al. 2015, ApJ, 808, 99
Reed, B. C. 2005, AJ, 130, 1652
Robitaille, T. P., & Whitney, B. A. 2010, ApJL, 710, L11
Roman-Duval, J., Heyer, M., Brunt, C. M., et al. 2016, ApJ, 818, 144
Russeil, D., Zavagno, A., Mège, P., et al. 2017, A&A, 601, L5
Schmidt, M. 1959, ApJ, 129, 243
Schruba, A., Leroy, A. K., Walter, F., et al. 2011, AJ, 142, 37
Smith, L. F., Biermann, P., & Mezger, P. G. 1978, A&A, 66, 65
Sofue, Y., & Nakanishi, H. 2017, PASJ, 69, 19
Soler, J. D., Miville-Deschênes, M. A., Molinari, S., et al. 2022, A&A, 662, A96
Traficante, A., Fuller, G. A., Billot, N., et al. 2017, MNRAS, 470, 3882
Urquhart, J. S., Moore, T. J. T., Csengeri, T., et al. 2014, MNRAS, 443, 1555
Veneziani, M., Elia, D., Noriega-Crespo, A., et al. 2013, A&A, 549, A130
Veneziani, M., Schisano, E., Elia, D., et al. 2017, A&A, 599, A7
Voskes, T., & Butler Burton, W. 2006, arXiv:astro-ph/0601653
Westerhout, G. 1957, Bull. Astron. Inst. Netherlands, 13, 201
Xiang, M., Shi, J., Liu, X., et al. 2018, ApJS, 237, 33
Yu, S.-Y., Ho, L. C., & Wang, J. 2021, ApJ, 917, 88
Yusef-Zadeh, F., Hewitt, J. W., Arendt, R. G., et al. 2009, ApJ, 702, 178